

NuSTAR HARD X-RAY DATA AND GEMINI 3D SPECTRA REVEAL POWERFUL AGN AND OUTFLOW HISTORIES IN TWO LOW-REDSHIFT LYMAN- α BLOBS

TAIKI KAWAMURO^{1,2}, MISCHA SCHIRMER³, JAMES E. H. TURNER³, REBECCA L. DAVIES⁴, AND KOHEI ICHIKAWA^{2,5,6}

Draft version November 7, 2018

ABSTRACT

We have shown that Lyman- α blobs (LABs) may still exist even at $z \sim 0.3$, about 7 billion years later than most other LABs known (Schirmer et al. 2016). Their luminous Ly α and [O III] emitters at $z \sim 0.3$ offer new insights into the ionization mechanism. This paper focuses on the two X-ray brightest LABs at $z \sim 0.3$, SDSS J0113+0106 (J0113) and SDSS J1155-0147 (J1155), comparable in size and luminosity to ‘B1’, one of the best-studied LABs at $z \gtrsim 2$. Our *NuSTAR* hard X-ray (3–30 keV) observations reveal powerful active galactic nuclei (AGN) with $L_{2-10 \text{ keV}} = (0.5-3) \times 10^{44} \text{ erg s}^{-1}$. J0113 also faded by a factor of ~ 5 between 2014 and 2016, emphasizing that variable AGN may cause apparent ionization deficits in LABs. Joint spectral analyses including *Chandra* data constrain column densities of $N_{\text{H}} = 5.1_{-3.3}^{+3.1} \times 10^{23} \text{ cm}^{-2}$ (J0113) and $N_{\text{H}} = 6.0_{-1.1}^{+1.4} \times 10^{22} \text{ cm}^{-2}$ (J1155). J0113 is likely buried in a torus with a narrow ionization cone, but ionizing radiation is also leaking in other directions as revealed by our Gemini/GMOS 3D spectroscopy. The latter shows a bipolar outflow over 10 kpc, with a peculiar velocity profile that is best explained by AGN flickering. X-ray analysis of J1155 reveals a weakly absorbed AGN that may ionize over a wide solid angle, consistent with our 3D spectra. Extinction corrected [O III] log-luminosities are high, ~ 43.6 . The velocity dispersions are low, $\sim 100-150 \text{ km s}^{-1}$, even at the AGN positions. We argue that this is a combination of high extinction hiding the turbulent gas, and previous outflows that have cleared the escape paths for their successors.

Subject headings: galaxies: active – galaxies: individual (SDSS J011341.11+010608.5, SDSS J115544.59-014739.9) – X-rays: galaxies

1. INTRODUCTION

Lyman- α blobs (LABs) are extended ($\sim 20-200 \text{ kpc}$) nebulae with luminosities of $L_{\text{Ly}\alpha} = 10^{42-44} \text{ erg s}^{-1}$. They are commonly found at redshifts $z \gtrsim 2$ in overdense regions and proto-clusters (Matsuda et al. 2011; Erb et al. 2011), and have been associated with a broad range of galaxies hosting active galactic nuclei (AGN), star-burst sub-mm galaxies, and passively evolving red galaxies (e.g. Francis et al. 2001; Matsuda et al. 2004; Geach et al. 2009; Bridge et al. 2013). LABs are landmarks of massive galaxy formation (Geach et al. 2005; Matsuda et al. 2006; Prescott et al. 2008), and this understanding would greatly benefit from studying the physical conditions and ionizing sources in LABs.

This, however, is difficult for several reasons. First, Ly α photons scatter resonantly in space and frequency (Meinköhn & Richling 2002; Verhamme et al. 2006; Kollmeier et al. 2010), and non-resonant diagnostic lines such as [O III] and H α must be used to study the physical conditions in the gas. Second, any emission lines in high- z LABs are faint because of se-

vere cosmological surface brightness dimming ($\propto (1+z)^{-4}$). Third, the lines may not be observable from the ground if their redshifted emission falls into the near-infrared atmospheric absorption bands. Fourth, the fraction of Ly α photons that manage to escape is controlled by dust, neutral hydrogen, metallicity, and outflows (Ciardullo et al. 2014; Henry et al. 2015; Rivera-Thorsen et al. 2015; Yang et al. 2016), a process that is still poorly understood.

Many LABs lack evidence of ionizing continuum sources that would explain their high Ly α luminosities. Three main ideas have been put forward to solve this mystery:

First, *the ionizing sources are spatially distributed*, i.e., Ly α is created by other processes, such as shock heating by starburst driven superwinds (e.g. Taniguchi & Shioya 2000), or gravitational cooling radiation of neutral hydrogen (‘cold accretion’, Haiman et al. 2000; Fardal et al. 2001; Nilsson et al. 2006; Rosdahl & Blaizot 2012).

Second, *the ionizing sources are hidden*, in particular obscured powerful AGN (Basu-Zych & Scharf 2004; Geach et al. 2009; Overzier et al. 2013; Prescott et al. 2015). It is difficult to distinguish between buried AGN and cold accretion (Prescott et al. 2015), and between cold accretion and scattering (Laursen & Sommer-Larsen 2007; Trebitsch et al. 2016), because the same data can be interpreted differently. Also, Steidel et al. (2000) and Schirmer et al. (2016) caution against postulating the presence of *obscured* AGN when evidence for other mechanisms is absent.

Third, *the ionizing sources (AGN) are variable*, and thus not detectable at all times (Schirmer et al. 2016).

¹ Department of Astronomy, Kyoto University, Kyoto 606-8502, Japan

² National Astronomical Observatory of Japan, Osawa, Mitaka, Tokyo 181-8588, Japan

³ Gemini Observatory, Southern Operations Center, Casilla 603, La Serena, Chile

⁴ Max-Planck-Institut für Extraterrestrische Physik, 85748 Garching, Germany

⁵ Department of Physics and Astronomy, University of Texas at San Antonio, One UTSA Circle, San Antonio, TX 78249, USA

⁶ Department of Astronomy, Columbia University, 550 West 120th Street, New York, NY 10027, USA

Accordingly, during their quasar phases, the AGN fill the LABs with Ly α photons; the latter are trapped because of resonant scattering and released only gradually. The observable Ly α light curve is thus a very damped response to the AGN’s ionizing light curve (Roy et al. 2010; Xu et al. 2011). Effectively, the Ly α and X-ray light curves are decorrelated. High Ly α luminosities therefore do not require *currently* powerful AGN (Schirmer et al. 2016), because AGN spend most of the time in a low accretion state (Novak et al. 2011). This may explain many of the non-detections of AGN that were originally attributed to heavy obscuration.

The existence of LABs at low redshift would provide exciting targets because of high fluxes and the full availability of optical diagnostic emission lines. Previous searches for LABs at $z \sim 0.7$ – 1.1 using *GALEX* grism spectroscopy were unsuccessful (Keel et al. 2009; Wold et al. 2014), apart from one detection by Barger et al. (2012) of a less luminous LAB ($L_{\text{Ly}\alpha} = 7.2 \times 10^{42} \text{ ergs}^{-1}$) at $z = 0.977$. These were first strong indications that LABs must rapidly disappear from the Universe between $z \sim 2$ and $z \sim 0.7$ (see Figure 6 in Schirmer et al. 2016). Overzier et al. (2013) have predicted that a small number of low- z LABs should still exist in low-density environments, mostly powered by AGN because cold accretion streams would have ceased. Indeed, in Schirmer et al. (2016) we have reported the discovery of rare, luminous LABs at $z \sim 0.3$ by cross-correlating the most powerful [O III] emitters of Schirmer et al. (2013) with archival *GALEX* far-UV images. *Hubble Space Telescope (HST)* far-UV images and spectra have been scheduled (PI: Schirmer, proposal ID #14749) to ultimately verify the Ly α luminosities.

As predicted in Section 4.2 of Overzier et al. (2013), Schirmer et al. (2013) confirmed that these low- z LABs are indeed powered by AGN from their high [O III]/H β line ratios. If a duty cycle of a luminous AGN phase is short as predicted by Novak et al. (2011), the majority of these AGN is likely to be weak. This idea corresponds to the third one raised previously. Hence, for the examination, we have analyzed the *Chandra* data, and found that the soft ($\lesssim 8 \text{ keV}$) X-ray luminosities are lower than expected (Schirmer et al. 2016). This apparently favors our hypothesis. However, due to the soft energy band and the poor photon statistics, the discussion highly depends on the assumed absorption correction. The AGN could simply be heavily obscured ($N_{\text{H}} \gtrsim 10^{24} \text{ cm}^{-2}$) rather than intrinsically weak. This has motivated us to conduct further X-ray observations at high energies to constrain the column densities and the *current* luminosities.

NuSTAR is the most sensitive observatory to hard X-rays ($> 10 \text{ keV}$), which are less affected by obscuration. Strong constraints on the luminosity can be obtained even for Compton-thick AGN ($N_{\text{H}} > 10^{24} \text{ cm}^{-2}$). Soft X-ray spectra of such AGN may be dominated by scattered and/or reflected components, and thus a joint spectral analysis of soft and hard X-ray data is required to accurately determine obscuration and luminosities. Using a pilot *NuSTAR* program, we observed the two *Chandra* brightest (and least likely faded) sources of Schirmer et al. (2016), SDSS J011341.11+010608.5 and SDSS J115544.59–014739.9 (hereafter J0113 and J1155).

This paper is organized as follows. Section 2 presents

an overview of our *NuSTAR*, *Chandra*, *Swift*, and Gemini observations. Details about the simultaneous analysis of the good quality *NuSTAR* and *Chandra* spectra and its results are found in Section 3. Results from the optical 3D spectra are presented in Section 4. In Section 5, we discuss the structures of the AGN, and the morphologies and kinematics of the extended emission line regions. We summarize and conclude in Section 6. Throughout this paper, we assume a Λ CDM cosmology with $H_0 = 70 \text{ km s}^{-1} \text{ Mpc}^{-1}$, $\Omega_{\text{m}} = 0.3$ and $\Omega_{\Lambda} = 0.7$. Unless otherwise noted, all errors concerning the X-ray data are quoted at the 90% confidence level for a single parameter of interest; errors for the optical data are 67% confidence level.

2. OBSERVATIONS AND DATA REDUCTION

Table 1 summarizes the basic information of the two LABs and the details on their *NuSTAR* (Harrison et al. 2013), *Chandra*, and *Swift* observations. The *NuSTAR* observations were conducted in cycle 2 as a Guest Observatory program (PI: Schirmer), followed by the *Swift* observations with short exposures (~ 1 – 2 ksec) as a service program. Also, *Chandra* observed J0113 (PI: Schirmer) and J1155 (PI: Coppi) in 2014 and 2002, respectively. We use the *Swift*/X-ray telescope (XRT; Gehrels et al. 2005) data reprocessed through the online tools provided by the UK *Swift* Science Data Centre (Evans et al. 2009)⁷. Due to the low signal-to-noise ratio of the *Swift* spectra (see Section 2.3), we perform the detailed analysis only for the *NuSTAR* and *Chandra* spectra (Figure 1). XSPEC version 12.9.0.n (Award 1996) is used for the spectral fitting.

The 3D Gemini/GMOS spectra are from a larger campaign targeting all 17 objects of Schirmer et al. (2016); details are given below.

2.1. *NuSTAR* Observations

NuSTAR carries two independent focal plane modules (FPMA and FPMB), sensitive in the 3–80 keV range. We reprocess the event files using the standard `nupipeline` script as described in the “*NuSTAR* Analysis Quickstart Guide”⁸. Our targets are faint ($\sim 10^{-3} \text{ cts s}^{-1}$), and periods of high background (such as passages through or near the South Atlantic Anomaly (SAA)) must be excluded. Typical background rates observed with *NuSTAR* are $\lesssim 1 \text{ cts s}^{-1}$, integrated over the focal plane (Forster et al. 2014). Times of high background can be identified by simultaneously increased count rates in the detectors as well as in the shields that surround the focal planes. Using the telemetry reports made by the *NuSTAR* team, we first check the total event rates during all orbital passages of our observations. In the J1155 observation, the event rate increases around the standard SAA area (above $\sim 30 \text{ cts s}^{-1}$). We run `nupipeline` with the option `saamode=optimized` to reject times with high count rates in both the shields and detectors. High count rates may occasionally occur in the so-called tentacle region (Forster et al. 2014) near the SAA, and we exclude these times for J1155 by setting `tentacle=yes`. Background rates during the observation of J0113 are stable and low (`saamode=none` and `tentacle=no`).

⁷ http://www.swift.ac.uk/user_objects/

⁸ http://www.srl.caltech.edu/NuSTAR_Public/NuSTAROperationSite/SAA_Fi

TABLE 1
BASIC TARGET INFORMATION

Name (1)	α_{J2000} (2)	δ_{J2000} (3)	z (4)	D (5)	Observatory (6)	ID (7)	Date (8)	Exp. (9)
SDSS J011341.11+010608.5	18.42129	1.10237	0.281	1.45	<i>NuSTAR</i>	60201054002	2016 July 01	21
					<i>Chandra</i>	16102	2014 Jun 02	15
					<i>Swift</i>	00081905001	2016 Jun 30	1.6
					Gemini/GMOS	GS-2016B-DD-4	2016 Nov 06	4.8
SDSS J115544.59-014739.9	178.93580	-1.79443	0.306	1.60	<i>NuSTAR</i>	60201055002	2016 Jun 07	20
					<i>Chandra</i>	3140	2002 Dec 02	30
					<i>Swift</i>	00081906001	2016 Jun 05	1.9
					Gemini/GMOS	GS-2014B-Q-63	2015 Mar 31	5.4

NOTE. — Columns: (1) Galaxy name. (2)-(3) Right Ascension and Declination in units of degree. (4) Redshift. (5) Luminosity distance in units of Gpc based on each redshift. (6) Observatory (7)-(9) Details for each observation (Obs. ID, Obs. date, and total exposure time in units of ksec).

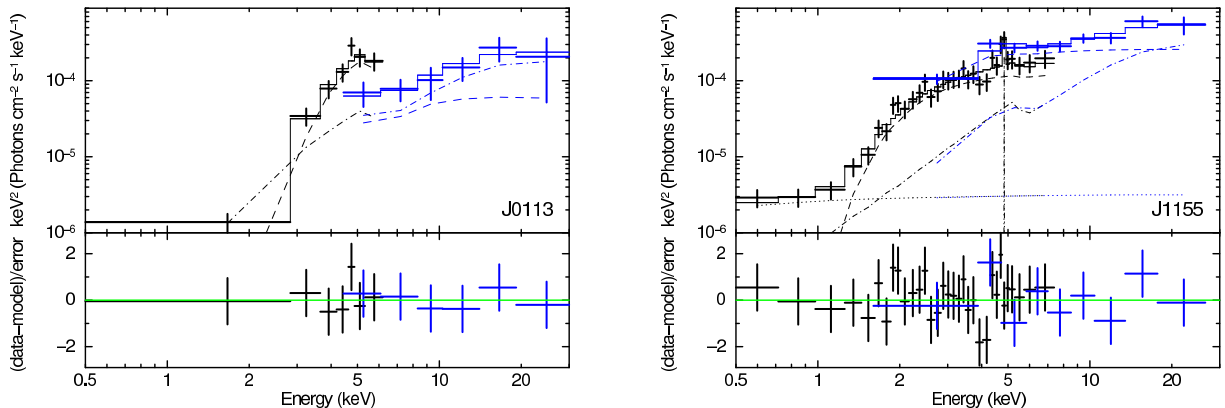


FIG. 1.— Unfolded broad-band spectra of J0113 (left) and J1155 (right). The *Chandra* and *NuSTAR* data are displayed with thick lines in black and blue, respectively. Overlaid thin lines are the best-fit model (solid line), the absorbed cut-off power-law component (dashed), the reflection component (dot-dashed), the scattered component (dotted), and the iron $K\alpha$ line (dot-dot-dashed). In the left, the scattered and iron- $K\alpha$ components cannot be seen because of their small contributions. The lower panels display the residuals between the data and the best-fit model.

The full width at half maximum (FWHM) of the *NuSTAR* point spread function is $\sim 20''$. The source spectra are extracted from circular regions with a radius of $1'$ centered on the centroid of the counts. The background spectra are extracted from identical apertures, located in an off-source region on the same detector. To increase the signal-to-noise ratios, the FPMA and FPMB spectra are combined without renormalization due to lack of statistical power in the count rates using the `addascaspec` command in `FTOOLS`. J0113 and J1155 are significantly detected in the 3–30 keV band with a signal-to-noise ratio of ~ 8 and 20, respectively.

2.2. *Chandra* Observations

The *Chandra*/ACIS data provide the soft energy band (0.5–10 keV) for the spectral analysis. The raw data are reprocessed by using the `chandra_repro` pipeline included in the *Chandra* Interactive Analysis of Observations (CIAO) software (version 4.8) and referring to the latest CALDB at the time (version 4.7.2). The typical angular resolution of *Chandra*/ACIS is $\sim 1''$. Our targets are barely resolved in the *Chandra* data, and no offsets are observed between the X-ray and [O III] peak emission (see Schirmer et al. 2016, for details). The source spectra were extracted from a circular region with $2''$ radius, centered on the *Chandra* detections. The background spectra are taken from similar off-source regions. Back-

ground correction is minimal, as the source count rates are ~ 100 times higher. Consequently, we detect J0113 and J1155 at the 11σ and 23σ levels, respectively, in the 0.5–10 keV band.

2.3. *Swift* Observations

We analyze the *Swift*/XRT spectra covering the soft energy band (0.3–10 keV). We find the low detection significances of 2.3σ and 3.6σ for J0113 and J1155, respectively. It is likely due to the low exposure and effective area. Thus, these spectra are ignored in the detailed broadband X-ray spectral analysis. Here, we only constrain the observed fluxes to confirm the consistency with those estimated from the *NuSTAR* spectra. The power-law model is fitted based on the C -statistics appropriate to low-counts spectra instead of the chi-squared method. The 2–10 keV fluxes are found to be $< 2.0 \times 10^{-13}$ erg $\text{cm}^{-2} \text{s}^{-1}$ for J0113 and $4.7^{+6.3}_{-2.9} \times 10^{-13}$ erg $\text{cm}^{-2} \text{s}^{-1}$ for J1155. They are in well agreement with those from the *NuSTAR* spectra (see Section 3 and Table 2).

2.4. *Gemini/GMOS* Observations

The 3D spectra were obtained using GMOS at the Gemini-South telescope in Chile, using the IFU-2 configuration. The $5''0 \times 7''0$ field of view is sampled with $0''.2$ fibers, and corresponds to 22×31 kpc at $z = 0.3$.

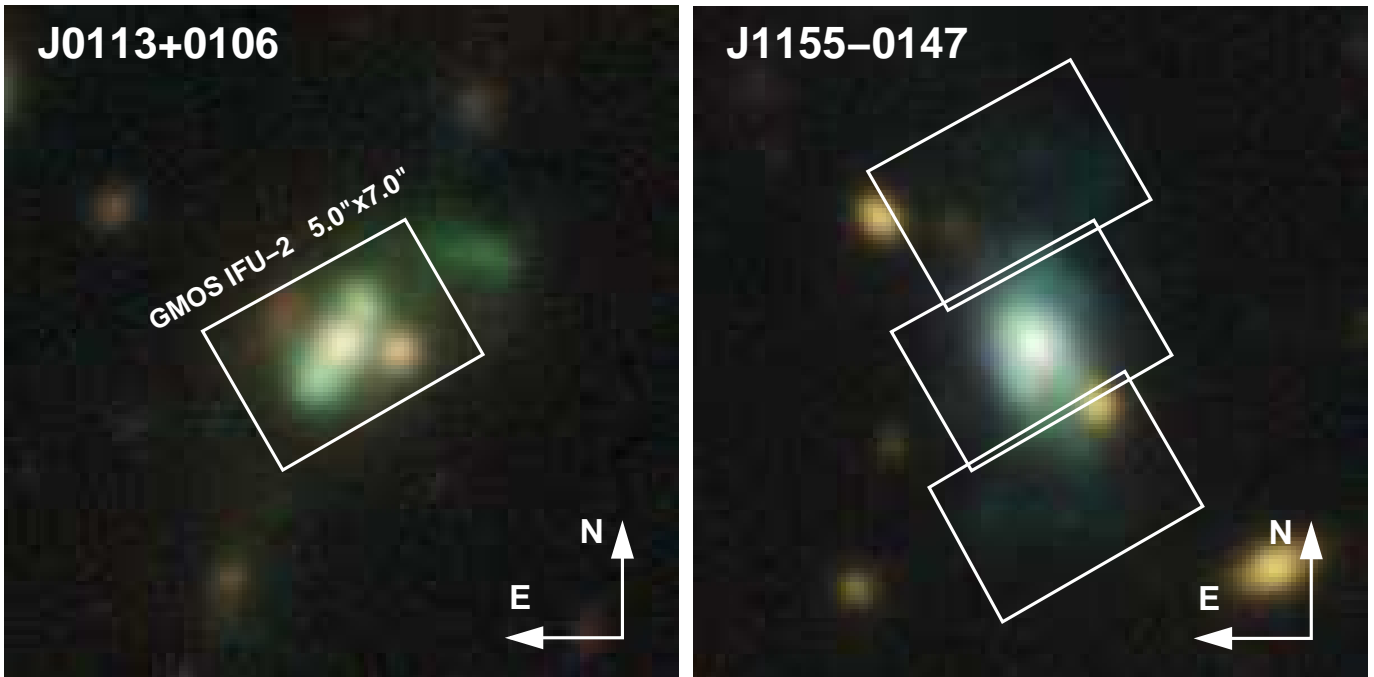


FIG. 2.— Layout of the GMOS 3D spectroscopy observations overlaid on GMOS *gri* color images, the latter measuring 93 and 99 kpc at the source redshifts of J0113 and J1155, respectively. Three pointings were used for J1155 to cover the full emission region. The [O III] emission dominates the *r*-band exposures, rendered green in these images. No offsets are observed between the *Chandra* detections and the peaks of the optical emission.

J0113 was observed on 2016 November 06 UT (Gemini program ID GS-2016B-DD-4) using 4×1200 s integrations in excellent seeing conditions ($0''.3$ – $0''.4$); the physical resolution corresponds to 1.5 kpc at $z = 0.281$. The pointing was centered on the nucleus and contains the bulk of the flux including the two superbubbles (see Figure 2, left panel). The [O III] $\lambda 5008$ line was compromised by a bad detector column that had developed around the time of the observations. The [O III] $\lambda 5008$ line luminosity and principal velocity structures could be reconstructed from the weaker [O III] $\lambda 4960$ line because of the fixed [O III] $\lambda 5008/4960$ line ratio of 2.984 (Storey & Zeppen 2000) and the good S/N ratio.

J1155 was observed on 2015 March 31 (GS-2014B-Q-63). Due to its large physical extent, three adjacent pointings were obtained with the IFU-2 (Figure 2, right panel), exposed for 2×900 s each, in $\sim 0''.7$ – $0''.8$ seeing conditions. The physical resolution is 3.5 kpc.

The spectra were processed using Python/IRAF scripts⁹ developed for GMOS IFU data. A detailed description of the reduction can be found in Davies et al. (2015) for SDSS J2240–0927, a low redshift LAB in our sample for which we have performed extensive emission line diagnostics.

The ionized gas kinematics were derived using the [O III] emission lines. For J1155 both the [O III] $\lambda 4960$ and [O III] $\lambda 5008$ lines were used. For J0113, the brighter [O III] $\lambda 5008$ line from half the IFU field of view was projected on a bad detector column and lost, and therefore only the weaker line was used. For each spaxel, a con-

stant continuum value was subtracted, and then each emission line was fit with a single Gaussian. If both lines were fit, then we used their fixed line ratio and required the same velocity and velocity dispersion.

3. BROADBAND X-RAY SPECTRAL ANALYSIS

Using XSPEC, we simultaneously fit the *Chandra* and *NuSTAR* spectra, which cover the 0.5–10 keV and 3–30 keV bands, respectively. The *Chandra* and *NuSTAR* spectra are binned so that each bin contains at least 15 cts and 100 cts, respectively, driven by the typical background rates. Bins are excluded from the spectral analysis if the source signal is below 1σ significance. The cross-normalization factor between the *Chandra* and *NuSTAR* spectra is set to one. We confirm that even if the factor is allowed to vary within a typical uncertainty of 10% (Harrison et al. 2013), the fitting results as well as the conclusion do not change significantly.

Following previous work by Kawamuro et al. (2016), who systematically analyzed broadband X-ray spectra of moderately obscured ($\log(N_{\text{H}}/\text{cm}^{-2}) = 22$ – 24) AGN, we adopt a base-line model,

$$F(E) = e^{-N_{\text{H}}\sigma(E)} P(E) + f_{\text{scat}} P(E) + R(E) + G(E) \quad (1)$$

in units of photons $\text{keV}^{-1} \text{cm}^{-2} \text{s}^{-1}$. Here, $\sigma(E)$ is the cross-section of photoelectric absorption at energy E . Our model uses a cutoff power-law for the absorbed primary X-ray emission, $P(E) \propto E^{-\Gamma} e^{-E/E_{\text{cut}}}$, where Γ is the photon index. The cutoff energy, E_{cut} , is difficult to constrain from the data, and thus fixed to 300 keV, a typical value measured in nearby AGN (Dadina 2008). The normalization of the primary emission between the *Chandra* and *NuSTAR* spectra are not tied to each other, due to the possible time variability between the two

⁹ Equivalent to the example available from the Gemini data reduction forum: drforum.gemini.edu/topic/gmos-ifu-data-reduction-example-2/

observations. An un-absorbed cutoff power-law model ($f_{\text{scat}}P(E)$) is also incorporated as scattered emission, where f_{scat} is the scattered fraction. The last two terms, $R(E)$ and $G(E)$, represent the reflection continuum from distant, cold matter (Urry & Padovani 1995, “torus”), and the accompanying fluorescence iron $K\alpha$ line at 6.4 keV, respectively. The torus’ reflection component is represented using the `pexrav` model (Magdziarz & Zdziarski 1995), which calculates reflected emission in an optically thick slab with a solid angle Ω irradiated by a point source. That is, $R_{\text{ref}} \equiv \Omega/2\pi = 2$ corresponds to the extreme case where the nucleus is covered by the reflector in all directions. Initially, the incident flux into the reflector is assumed to be the same as the primary power-law component of the *NuSTAR* spectra. The inclination angle to the reflector is fixed at 60° . We confirm that even for 30° the best-fit parameters do not change significantly. We assume that the reflected and scattered components did not vary between the *Chandra* and *NuSTAR* observations. The scattering/reflecting matter could be spatially distributed and extend to the pc scale. This suggests that even if the incident emission from the nucleus varies, the scattered/reflected emission does not change drastically because such matter smears the variability. The $K\alpha$ line is described using the delta function (`zgauss` with the line width of 0 eV in `XSPEC`). This is because the poor photon statistics and the low instrumental energy resolution do not permit an estimate. The galactic absorption, $N_{\text{H}}^{\text{gal}}$, is calculated using the `nh` command in `FTOOLS` (Kalberla et al. 2005), and is applied to the total base-line model.

In the following subsections we describe the details of the spectral analysis. The unfolded spectra and best-fit models are shown in Figure 1. The best-fit parameters, observed fluxes, and primary power-law luminosities are listed in Table 2. To estimate luminosity errors, we make confidence contours between the normalization and photon index of the primary power-law component (Figure 3). Then, we derive the upper and lower boundaries by calculating all the possible luminosities along the contours at the 90% confidence level.

3.1. Notes on J0113

The base-line model fits the spectra with $\chi^2/\text{d.o.f} = 3.3/6$. The AGN in J0113 is heavily obscured with a hydrogen column density of $N_{\text{H}} = 5.1^{+3.1}_{-3.3} \times 10^{23} \text{ cm}^{-2}$, and we find $\Gamma = 2.1^{+0.5}_{-1.2}$. The $K\alpha$ line and the scattered emission are insignificant, and their upper limits are constrained to be $A_{K\alpha} < 2.2 \times 10^{-6} \text{ photons cm}^{-2} \text{ s}^{-1}$ ($< 1.3 \times 10^{-14} \text{ erg cm}^{-2} \text{ s}^{-1}$) and $f_{\text{scat}} < 9.9\%$, respectively. The reflection strength is estimated to be $R_{\text{ref}} = 2.7$. If we assume that the incident flux into the reflecting and scattering material is based on the primary X-ray emission in the *Chandra* spectrum (instead of *NuSTAR*), then $R_{\text{ref}} \sim 0.5$ and $f_{\text{scat}} \lesssim 4\%$. Due to the poor statistics, the best-fit parameters in both cases are consistent with each other.

From the confidence contours in Figure 3, the intrinsic luminosities during the *Chandra* and *NuSTAR* observations are $\log(L_{2-10 \text{ keV}}/\text{erg s}^{-1}) = 44.5^{+0.5}_{-0.6}$ and 43.7 ± 0.8 , respectively (90% confidence errors on the luminosities). This AGN has likely faded by one order of magnitude in two years.

TABLE 2
BEST-FIT PARAMETERS

(1)	Name	J0113	J1155
(2)	$N_{\text{H}}^{\text{Gal}} (\times 10^{20})$	3.03	2.04
(3)	$N_{\text{H}} (\times 10^{22})$	51^{+31}_{-33}	$6.0^{+1.4}_{-1.1}$
(4)	Γ	$2.1^{+0.5}_{-1.2}$	$1.9^{+0.3}_{-0.4}$
(5)	$A_{\text{PL}}^{\text{Chandra}} (\times 10^{-4})$	$9.0^{+29.0}_{-8.8}$	$1.9^{+0.9}_{-0.8}$
(6)	$A_{\text{PL}}^{\text{NuSTAR}} (\times 10^{-4})$	$1.6^{+11.0}_{-1.0}$	$3.8^{+2.6}_{-1.9}$
(7)	f_{scat}	< 9.9	$1.2^{+1.6}_{-0.9}$
(8)	$A_{K\alpha} (\times 10^{-6})$	< 2.2	1.9 ± 1.3
(9)	R_{ref}	2.7*	1.0(< 2.5)
(10)	$F_{2-10}^{\text{Chandra}} (\times 10^{-13})$	3.6	3.6
(11)	$F_{2-10}^{\text{NuSTAR}} (\times 10^{-13})$	1.3	6.1
(12)	$\log L_{2-10}^{\text{Chandra}}$	$44.5^{+0.5}_{-0.6}$	$44.0^{+0.1}_{-0.2}$
(13)	$\log L_{2-10}^{\text{NuSTAR}}$	43.7 ± 0.8	44.3 ± 0.1
(14)	$\chi^2/\text{d.o.f.}$	3.3/6	28.9/35
(15)	<i>NuSTAR</i> cts (src/bg)	212/451	797/717
(16)	<i>Chandra</i> cts (src/bg)	117/1	526/1

NOTE. — Columns: (1) Galaxy name. (2) Galactic absorption in units of cm^{-2} . (3) Intrinsic absorption in units of cm^{-2} . (4) Photon index of the power-law component. (5)–(6) Photon fluxes in units of photons $\text{keV}^{-1} \text{ cm}^{-2} \text{ s}^{-1}$ at 1 keV of the primary power-law component in the *Chandra* and *NuSTAR* spectra, (7) Scattered fraction in units of %. (8) Total photon flux in the `zgauss` model in units of total photons $\text{cm}^{-2} \text{ s}^{-1}$. (9) Reflection strength defined as $R_{\text{ref}} = 2\pi/\Omega$ in the `pexrav` model. (10)–(11) Observed fluxes in the 2–10 keV band in units of $\text{erg cm}^{-2} \text{ s}^{-1}$. (12)–(13) Intrinsic (primary power-law component) luminosities at the galaxy rest frame in the 2–10 keV band. (14) Reduced chi-squared over degrees of freedom. (15)–(16) Source and background counts in the *NuSTAR* 3–30 keV and *Chandra* 0.5–10 keV bands. * The error at the 90% confidence level cannot be constrained within a range, where we allowed the parameter to vary ($R_{\text{ref}} = 0$ –10).

3.2. Notes on J1155

The base-line model reproduces the spectra well with $\chi^2/\text{d.o.f} = 28.9/35$. We find $\Gamma = 1.9^{+0.3}_{-0.4}$ and $N_{\text{H}} = 6.0^{+1.4}_{-1.1} \times 10^{22} \text{ cm}^{-2}$. The $K\alpha$ line is detected at the 90% confidence level with $A_{K\alpha} = (1.9 \pm 1.3) \times 10^{-6} \text{ photons cm}^{-2} \text{ s}^{-1}$, or $(1.9 \pm 1.4) \times 10^{-14} \text{ erg cm}^{-2} \text{ s}^{-1}$. This supports the existence of a torus. Although the spectra do not require the reflection continuum (`pexrav`) significantly as $R_{\text{ref}} = 1.0$ (< 2.5), this continuum emission should be taken into consideration to explain the $K\alpha$ line in a self-consistent way. The scattered emission is significantly detected below 1 keV, and the scattering fraction is $f_{\text{scat}} = 1.2^{+1.6}_{-0.9}\%$. This falls within a typical range of obscured Seyfert galaxies (0.1–10%; e.g., Kawamuro et al. 2016). Note that R_{ref} and f_{scat} with respect to the primary emission in the *Chandra* spectrum are $R_{\text{ref}} \approx 2$ and $f_{\text{scat}} \approx 2\%$, consistent with those derived above within uncertainties. Analogously to J0113, we find $\log(L_{2-10 \text{ keV}}/\text{erg s}^{-1}) = 44.0^{+0.1}_{-0.2}$ and 44.3 ± 0.1 for the epochs of the *Chandra* and *NuSTAR* observations, respectively. This AGN has brightened slightly between 2002 and 2016.

4. ANALYSIS OF THE OPTICAL 3D SPECTRA

4.1. J0113: [O III] and $H\beta$ luminosities

J0113 extends over $7'' \times 13''$, featuring two prominent superbubbles at a projected distance of 5 kpc on either side of the nucleus. The bubbles have a diameter of 5–8 kpc, each. A further outflow is found 24 kpc (North-

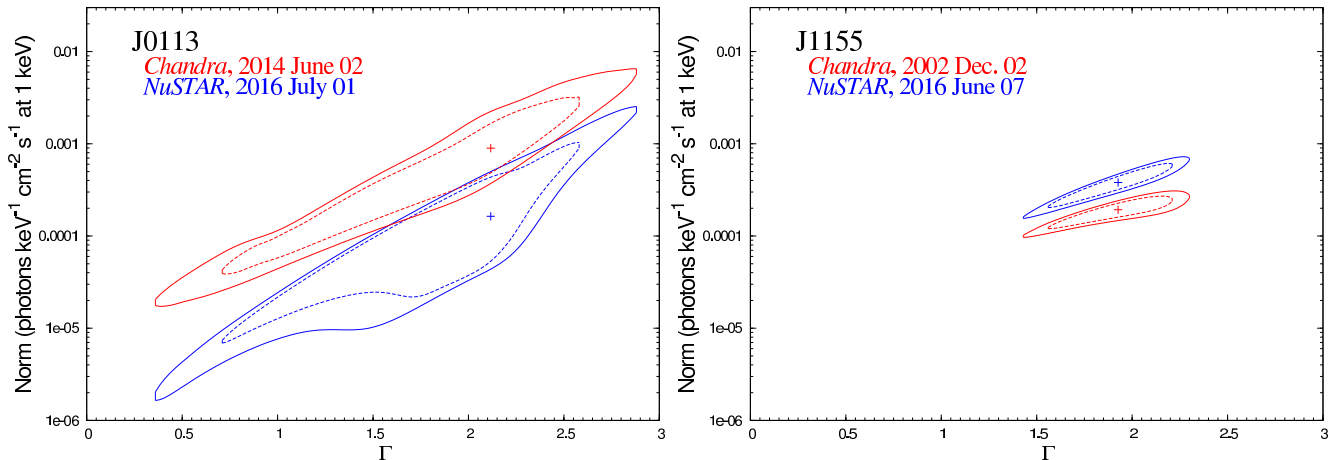


FIG. 3.— Confidence contours between the normalization and photon index of the primary power-law component based on the simultaneous fit to the spectra from *NuSTAR* (blue) and *Chandra* (red). While each cross denotes the best-fit value, the 68% and 90% confidence constraints are represented with the dashed and solid lines, respectively.

West) from the nucleus and measures 14 kpc. Judging from its r -band brightness and the [O III] equivalent line width of the central region, this outflow contributes 15–20% to the total [O III] luminosity, which we disregard in the further analysis. For more details see Figure 2 in this paper, and Appendix A4 in Schirmer et al. (2016).

The total [O III] λ 5008 flux in the IFU-2 data is $(4.36 \pm 0.44) \times 10^{-14}$ erg cm $^{-2}$ s $^{-1}$, equivalent to an observed (reddened) luminosity of 1.1×10^{43} erg s $^{-1}$. The archival spectrum from the Sloan Digital Sky Survey (SDSS) has a mean global $H\alpha/H\beta$ line ratio (Balmer decrement) of 4.4, indicative of significant dust extinction. Using a standard $R = 3.1$ dust extinction curve (Cardelli et al. 1989; Osterbrock & Ferland 2006), an intrinsic $H\alpha/H\beta$ line ratio of 3.0, we find $\log(L_{[\text{O III}]^c}^c/\text{erg s}^{-1}) = 43.6 \pm 0.1$ for the dereddened luminosity. Likewise, we measure a corrected $H\beta$ line luminosity of $\log(L_{H\beta}^c/\text{erg s}^{-1}) = 42.9 \pm 0.1$. The 1σ errors include the uncertainty of the flux calibration and allow for a relative uncertainty of 10% in the intrinsic $H\alpha/H\beta$ line ratio; the latter is subject to metallicity and hardness of the ionizing spectrum (Gaskell & Ferland 1984). Possible variations of the internal dust extinction remained unaccounted for because we do not have resolved $H\alpha$ maps at hand (for examples see Schirmer et al. 2013; Davies et al. 2015).

4.2. J0113: Gas kinematics

The kinematic maps in Figure 4 reveal a bipolar outflow. Relative radial velocities increase linearly from the nucleus to about 120 km s $^{-1}$ at the position of both superbubbles at 5 kpc distance. The Northern superbubble is blue-shifted, and the Southern bubble redshifted. Velocities then continue to increase in the same fashion beyond the bubbles, exceeding 200 km s $^{-1}$ at 10 kpc from the nucleus, where the S/N becomes too low for our analysis. The outflow does not appear to encounter significant mechanical resistance from the interstellar medium, and its motion is not yet governed by gravitation. The measured radial velocity is fairly low, suggesting that most of the motion happens perpendicular to our line-of-sight.

Another feature is that the gas South-West (North-

East) of the nucleus is redshifted (blueshifted). This velocity gradient is perpendicular to the outflow and with a lower amplitude of about 70 km s $^{-1}$. There is no indication of an outflow in this direction, and we interpret this as rotational motion of the central cloud of ionized gas.

The velocity dispersion is low (Figure 4, upper middle), and it is remarkable that the nucleus is not detectable in this map. We note a band of increased dispersion, 150–180 km s $^{-1}$, that appears to gird the nucleus and the bipolar outflow near its equatorial plane. In the two superbubbles and beyond, the dispersion drops to $\lesssim 100$ km s $^{-1}$, lower than in other outflow systems. We discuss these properties in Sections 5.2.3 and 5.2.4.

4.3. J1155: [O III] and $H\beta$ luminosities

J1155 has the highest X-ray flux in our sample. The optical nebula in the *gri* broadband images of Schirmer et al. (2016) extend over $9'' \times 19''$ or more than 60 kpc, and fragments into numerous smaller clouds of 3–7 kpc diameter scattered around a very bright center measuring 5 kpc in diameter. For more details see Figure 2 in this paper, and Appendix A6 in Schirmer et al. (2016).

We have no spectrum yet of J1155 that includes the $H\alpha$ line, and therefore we cannot determine a dereddened [O III] luminosity. The observed total line flux including calibration errors is $(8.0 \pm 0.8) \times 10^{-14}$ erg cm $^{-2}$ s $^{-1}$, corresponding to $\log(L_{[\text{O III}]}/\text{erg s}^{-1}) = 43.4 \pm 0.05$. If the Balmer decrement was a moderate 3.5, then $\log(L_{[\text{O III}]^c}^c/\text{erg s}^{-1}) = 43.6 \pm 0.1$ and $\log(L_{H\beta}^c/\text{erg s}^{-1}) = 42.5 \pm 0.1$. If the Balmer decrement was as high as for J0113, then $\log(L_{[\text{O III}]^c}^c/\text{erg s}^{-1}) = 43.9 \pm 0.1$. For the rest of this paper we adopt the more conservative, lower luminosities associated with less extinction.

4.4. J1155: Gas kinematics

J1155 has a very complex kinematic structure and [O III] morphology. The line emission is strongly concentrated in the center of the galaxy, and with low ve-

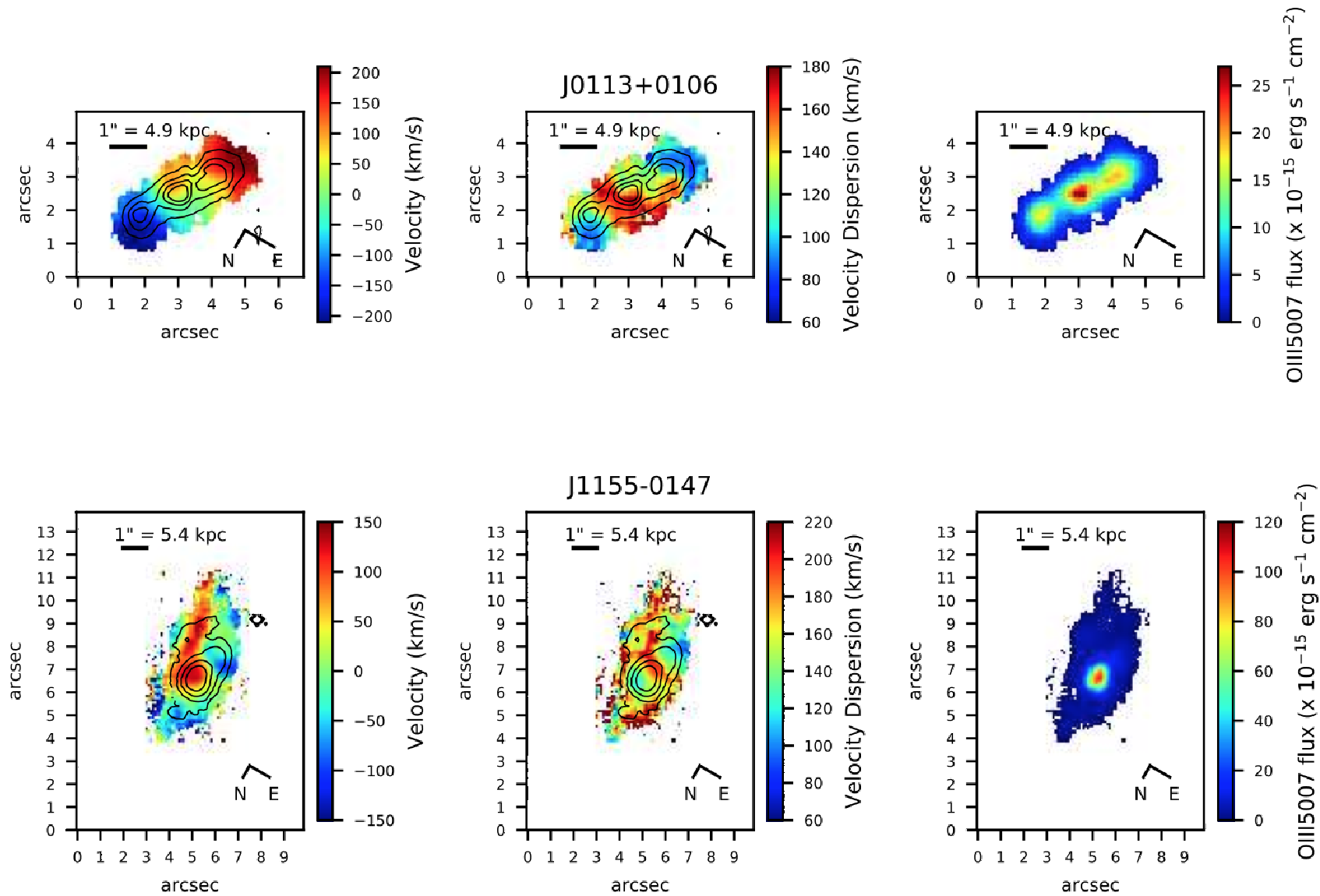


FIG. 4.— Gas velocity (left), velocity dispersion (center) and line flux (right) for J0113 (top) and J1155 (bottom). The line flux is also overplotted by the black contours in the velocity and dispersion panels. J0113 is dominated by a bipolar outflow, and a central cloud of rotating gas. The outflow axis and the rotation axis are aligned. J1155 has a very concentrated line flux and drives a narrow outflow over 20 kpc, with constant radial velocity. The masking corresponds to approximately a S/N cut of 5. Our IFU data are comparatively shallow; the gas in J0113 extends well beyond the plot frame, and the gas in J1155 fills the frame.

locity dispersion. Ionized gas extends out to ~ 25 kpc in these shallow IFU data, creating a patchy appearance and complex velocity and velocity dispersion maps. Particularly interesting is a long stream of gas connected to one side of the nucleus, stretching over 20 kpc and receding with a constant radial velocity of ~ 120 km s $^{-1}$. The width of the stream is barely resolved in the data (Figure 4, lower left); the velocity dispersion is increased further away from the nucleus. The remainder of the surrounding gas appears to be passively illuminated by the AGN.

Like J0113, the velocity dispersion in J1155 is fairly low, between 100–200 km s $^{-1}$ across the entire analysis area of 30×15 kpc. The nucleus is also not detectable (Figure 4, lower middle).

5. DISCUSSION

5.1. X-ray properties

5.1.1. Constraint on X-ray luminosity

Chandra is sensitive to soft energy X-ray photons in the ~ 0.7 –9 keV restframe for objects at $z \sim 0.3$. Hence, it is difficult to put a strong constraint on the intrinsic luminosity when the source is highly obscured. To show this fact, we derive luminosity errors in the case of that only the *Chandra* spectrum is available. As an example, we consider the J0113 case. We apply the same method as described in Section 3 to the error calculation except for allowing the absorbing column density to change up to $\log N_{\text{H}} = 24$ in the fitting to avoid extreme case. The resultant lower and upper boundaries of the primary power-law luminosity become -0.8 dex and $+1.5$ dex. These uncertainties are larger than obtained with the simultaneous fitting to the *NuSTAR* and *Chandra* spectra (-0.6 dex and $+0.5$ dex) possibly because the absorption column density is not well determined. This shows that the additional *NuSTAR* spectrum plays an important role to constrain the luminosity.

5.1.2. Narrow iron-K α line

The narrow K α line at ≈ 6.4 keV may originate from the torus around the nucleus, and was detected significantly only for J1155. Its equivalent width with respect to the reflection continuum is $\text{EW} = 760_{-580}^{+830}$ eV ($\text{EW} < 7900$ eV for J0113). Here, only an uncertainty of the iron line flux is incorporated into the error calculation because the lower limit of the reflection strength is not constrained. The EWs are consistent with a numerical calculation of the reflected emission for optically thick, cold matter (1–2 keV; Matt et al. 1991). On the other hand, the EWs of J0113 against the total continuum observed with *Chandra* and *NuSTAR* are < 240 eV and < 740 eV, whereas those of J1155 are 210 eV and 130 eV, respectively. All observed EWs are consistent with those found in typical obscured AGN (e.g., Brightman & Nandra 2011; Kawamuro et al. 2016). We conclude that our low- z LABs and typical Seyfert galaxies may have the same origin of the K α line.

5.1.3. Scattering fraction

We observe significant scattered emission ($f_{\text{scat}} \sim 1.2\%$) for J1155, which implies that J1155 is not heavily buried in the dust or gas obscuration. In comparison,

heavily buried AGN (as suggested from their strong reflected emission) show rather low scattering fractions of $f_{\text{scat}} < 0.5\%$ (e.g. Ueda et al. 2007; Eguchi et al. 2009). We conclude that the emission from the nucleus in J1155 is relatively unobscured, and that the AGN contributes over a large solid angle to the ionization of the LAB.

By contrast, we cannot find significant scattered emission in J0113 ($f_{\text{scat}} < 9.9\%$), suggesting the presence of a buried AGN and also a smaller contribution to the ionization.

5.2. Properties from the optical 3D spectra

5.2.1. Comparison samples

How are the galaxy-scale outflows in this study different from other systems with similar properties? Our targets were selected from SDSS-DR8 (Aihara et al. 2011) solely based on their broad-band photometry (excess of r -band flux due to redshifted, very high [O III] emission at $z \sim 0.3$). We also applied a lower threshold on their radius to select objects with extended outflows. Both our targets are radio-quiet and ionized by type-2 AGN (Schirmer et al. 2013).

We compare with the 16 radio-quiet type-2 AGN of Harrison et al. (2014), selected from SDSS because of their high spectroscopic [O III] $\lambda 5008$ flux. Harrison et al. (2014) also required the presence of a broad [O III] component. Typical redshifts are $z \sim 0.1$. Our other comparison sample is that of Liu et al. (2013), who selected 11 type-2 AGN with galaxy-scale outflows (at $z \sim 0.5$) in SDSS based on high [O III] fluxes. Liu et al. (2013) complement their sample with 3 radio-loud AGN to study the impact of jets on the outflow systems. Like us, Harrison et al. (2014) and Liu et al. (2013) used Gemini/GMOS to obtain the 3D spectra, in comparable seeing conditions. The depth of the spectra are approximately similar to ours of J0113. Our data of J1155 is much shallower though, by about a factor ~ 10 in effective exposure time (short integrations; full moon, compared to dark sky conditions for the comparison data).

5.2.2. Ionized gas mass

We derived H β logarithmic line luminosities of 42.9 and 42.5 for J0113 and J1155, respectively (Sections 4.1 and 4.3). Assuming the gas is purely photoionized, the gas mass M associated with the H β emission is estimated as

$$M = \frac{L_{\text{H}\beta}}{4\pi j_{\text{H}\beta}} n_e m_p, \quad (2)$$

where $4\pi j_{\text{H}\beta}$ is the emission per unit volume, n_e the electron number density and m_p the proton mass. Taking $4\pi j_{\text{H}\beta}$ from Osterbrock & Ferland (2006) (their table 4.4; see also Storey & Sochi 2015) for $T = 10^4$ K and $n_e = 100$ cm $^{-3}$, we rewrite

$$M = 6.77 \times 10^8 M_{\odot} \frac{L_{\text{H}\beta}}{10^{43} \text{ erg s}^{-1}} \left(\frac{n_e}{100 \text{ cm}^{-3}} \right)^{-1}. \quad (3)$$

Individual measurements of n_e , derived from the [S II] $\lambda 6719,33$ line ratio, yield several 100 cm $^{-3}$ in the inner regions of narrow-line regions (see e.g. Nesvadba et al. 2006; Davies et al. 2015). Using line ratios which are sensitive at higher densities, $n_e \sim 10^3$

(10^{4-5}) cm^{-3} were found for the narrow (broad) lines of another luminous quasar (Holt et al. 2011). In the outskirts, densities drop below 100 cm^{-3} , where the outflows have thinned and are difficult to detect (and where line ratio methods break down because the collision effects diminish). Our spectrum of J0113 does not include the [S II] doublet; however, there is an SDSS spectrum taken with a $3''$ fiber centered on the nucleus, including the flux from the nucleus and most of the superbubbles. Fitting the [S II] doublet with a simple double Gaussian with identical line widths, we derive a line ratio of 1.24, i.e., a mean $n_e \sim 180 \text{ cm}^{-3}$. We expect the actual electron densities to deviate significantly from this number, because outflows are known to be clumpy (Nesvadba et al. 2006; Greene et al. 2011; Davies et al. 2015).

Using eq. (3), we find $5.4 \times 10^8 M_\odot$ and $2.0 \times 10^8 M_\odot$ for J0113 and J1155, respectively, for a fixed value of $n_e = 100 \text{ cm}^{-3}$. This is near the upper end of the gas masses of $(0.2-4) \times 10^8 M_\odot$ found by Harrison et al. (2014), using the same density normalization. The outflows of Liu et al. (2013) entrain higher masses, $(2-10) \times 10^8 M_\odot$ (again for $n_e = 100 \text{ cm}^{-3}$).

We note that Harrison et al. (2014) and Liu et al. (2013) have a numeric prefactor that is erroneously about a factor 4 too high compared to ours in eq. (3). This is caused by an incorrect calculation of the recombination coefficient $\alpha_{\text{H}\alpha}^{\text{eff}}$ in eq. (1) of Nesvadba et al. (2006) (N. Nesvadba, private communication). Taking this into account, the ionized gas masses of J0113 and J1155 are among the highest measured in type-2 AGN at $z \lesssim 0.6$.

5.2.3. Gas velocities

Assuming a typical, true outflow velocity of 1000 km s^{-1} for the [O III] gas (Harrison et al. 2014), it would take the two superbubbles in J0113 at least $\sim 10^7$ years to reach their observed positions. However, a sustained high AGN output over such a long time is implausible, as single AGN duty cycles are expected to be comparatively short (10^{4-6} yr; e.g., Schawinski et al. 2010; Schawinski et al. 2015; Sun et al. 2017) and followed by longer low states.

What happens with such an outflow during the low states of the AGN? King et al. (2011) calculate the internal properties of outflows and their dynamics. They find that the thermal energy contained in an energy-driven outflow can support its expansion for periods 10 times longer than the actual quasar phase that launched the outflow. However, their numerical results do not show that the velocity in such a stream is increasing over kpc-scales from the nucleus, as we observe in J0113. In a more recent work, Zubovas & King (2016) study the evolution of outflows taking into account recurrent AGN duty cycles lasting 5×10^4 years. In these calculations, the recurrent duty cycles manage to accelerate existing outflows after about $\sim 10^6$ years, and out to radii larger than 10 kpc. Zubovas & King (2016) also find that the AGN should switch off once sufficient energy has been injected to unbind all gas; this is not (yet) the case in J0113 as our X-ray observations still reveal a very powerful AGN (one that has albeit likely faded in the last two years). Other processes could also explain the apparent acceleration. J0113 is weakly detected in the radio VLA FIRST survey (1.18 mJy; Schirmer et al. 2013), suggesting that a

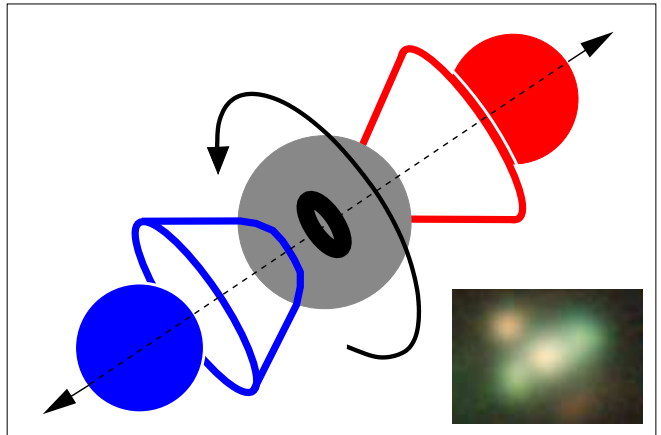


FIG. 5.— Model of J0113, showing the system’s orientation, outflow geometry and main kinematics in our IFU data. The blue and red spheres illustrate the approaching and receding superbubbles, respectively. The gray sphere represents the central ionized cloud of gas that rotates in the direction indicated. The rotation axis coincides with the direction of the outflow. The AGN is obscured from our view by a dusty torus. The two half cones indicate how the system lies in the plane of the sky (they are not meant to represent ionization cones). The inset shows the optical GMOS image in gri filters.

former radio jet could have played a role in shaping the current velocity profile. However, the survey’s spatial resolution and depth (White et al. 1997) are insufficient for further conclusions. Alternatively, differential velocities in the stream could be at play (faster components reach further in the same amount of time). However, Liu et al. (2013) argue that in this case the velocity dispersion should increase as well with increasing distance, yet we observe a decrease in dispersion. We conclude that with the current data at hand, recurrent outflows are the best explanation for the peculiar velocity profile in the outflow of J0113.

Faucher-Giguère & Quataert (2012) have shown that an outflow preferentially breaks out from a denser disk or sphere along paths of least resistance. The hot buoyant gas would then inflate the bubbles, and bipolar systems should be produced eventually by many powerful AGN. J0113 seems prototypical in this respect; we condense our observational results in a simplistic graphical representation in Figure 5.

J1155, on the other hand, could not be more different. While we do trace a 20 kpc long linear feature of enhanced recession velocity (Figure 4, lower left), it is not particularly present in the line flux map (Figure 4, lower right). The [O III] nebula fragments into numerous blobs at all azimuthal angles around the AGN, which do not appear to be connected to any currently active outflow, nor to any of the member galaxies of the small group that hosts J1155 in its center (see also Section 5.2.4 and Figure 2). We think that J1155 represents a more advanced stage, where the ejected materials from various duty cycles have accumulated in the halo, but have not yet fully dispersed. Currently, J1155 experiences another powerful accretion event, as indicated by the very high central [OIII] surface brightness and its high X-ray luminosity.

5.2.4. Velocity dispersion

What comes to attention with our IFU data are the fairly low velocity dispersions in both systems, in partic-

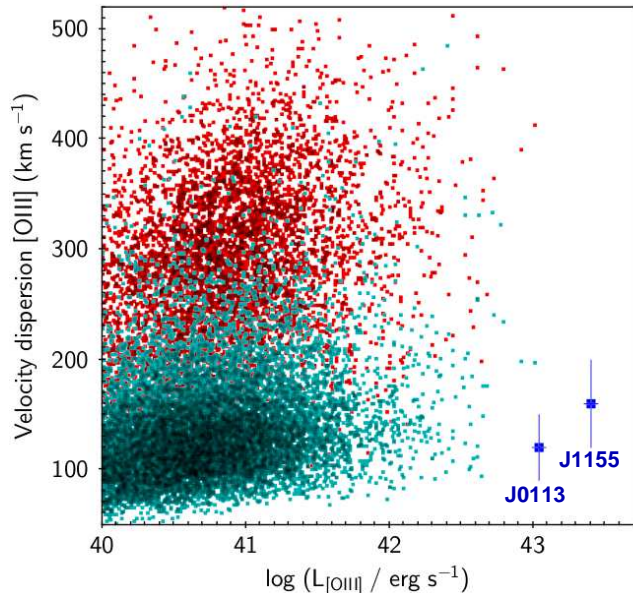


FIG. 6.— [O III] velocity dispersion versus (reddened) luminosity for the type-2 AGN sample of Mullaney et al. (2013). The bright blue and red data clouds represent the narrow and broad components, respectively, of the line fits by Mullaney et al. (2013). Overplotted are our two targets, where the vertical error bars represent the actual scattering over the IFU field of view. J0113 and J1155 have higher observed [O III] luminosities than any other type-2 AGN in the comparison sample, and broad line components are absent in them. Note that Mullaney et al. (2013) originally reported the lines’ FWHM; for comparison with our data we converted them to velocity dispersions assuming Gaussian line profiles.

ular for their nuclei (see Figure 4). Near the center of J0113 we observe 150–180 km s⁻¹, and for the two superbubbles and beyond the dispersion drops to 100 km s⁻¹ and below. For J1155, we observe a mean dispersion of 160 km s⁻¹. In Figure 6 we compare our targets against the type-2 sample of Mullaney et al. (2013). We recall that our data of J1155 are shallow, and therefore any broad components in the outskirts of this nebula would remain undetected; consequently, we would underestimate its line FWHM.

The low velocity dispersions show that the gas is little turbulent, in particular for J0113. There, it is flowing away from the AGN in a radial fashion, probably still pushed by recurrent duty cycles and its internal thermal energy. If powerful earlier outflows have “cleared” the escape path already, then the current stream would find less resistance and thus be less turbulent. Indeed, our imaging data show the presence of older outflows that must have traveled along the same paths.

Liu et al. (2013) find high (~ 500 – 1500 km s⁻¹) velocity dispersions in the inner 5–10 kpc of their sample, which in about half of the cases drop to 100–200 km s⁻¹ at 10–15 kpc distance. Like us, they argue that recurrent outflows could have cleared the escape path. Additionally, Liu et al. (2013) explain that the narrow opening angle of the outflow (once it managed to break out) would leave less space for projected velocities, naturally decreasing the observed velocity dispersions. A noticeable difference between their and our data is that J0113 and J1155 have low velocity dispersions *everywhere*, even near the nucleus (our data of J0113 has a physical resolution of 1.5 kpc). Perhaps the more turbu-

lent central components are simply hidden by dust. The enhanced Balmer decrement of 4.4 (integrated over 15 kpc by the SDSS fiber) shows that at least some part of the ionized gas must be severely affected by absorption, which goes in line with the high column density of $N_{\text{H}}/\text{cm}^2 = 5.1 \times 10^{23} \text{ cm}^{-2}$ (J0113).

J1155 also reveals a rather low velocity dispersion, about 160 km s⁻¹ averaged over our IFU data. Hardly any of its numerous extended features appear to be connected to actively driven outflows. This material was probably ejected during several AGN bursts in the past, and is now passively ionized by the AGN. A notable environmental difference with respect to J0113 is that J1155 is not isolated, but located at the center of a small galaxy group with $M_{200} \sim 1.3 \times 10^{13} M_{\odot}$. Schirmer et al. (2016) speculated that the unusual morphology of this system could be due to interaction with infalling gas from an intragroup medium (undetected in X-rays). Alternatively, the surrounding inner material could have a lower filling factor, offering more escape paths for any buoyant hot gas. That would also be consistent with the lower absorbing X-ray column density.

5.3. Comparison with the high-*z* LAB ‘B1’

One of the best-studied (and most luminous) LABs is SDSS J2143–4423 (also known as ‘B1’, $z = 2.38$). Its Ly α emission extends over 30×100 kpc (Francis et al. 2001), and Palunas et al. (2004) report a Ly α line flux of $1.35 \times 10^{-15} \text{ erg cm}^{-2} \text{ s}^{-1}$, or $\log(L_{\text{Ly}\alpha}/\text{erg s}^{-1}) = 43.8$. Overzier et al. (2013) measure a dereddened [O III] luminosity of $\log(L_{[\text{O III}]}/\text{erg s}^{-1}) = 43.4$ – 44.1 , subject to uncertain extinction correction. The optical nebula extends over 32×40 kpc. The [O III] line FWHM within 10 kpc of the nucleus is 600–800 km s⁻¹, and drops to 200 km s⁻¹ beyond 10 kpc (similar to many of the targets studied by Liu et al. 2013). The radial gas velocities in B1 are low, mostly within ± 50 km s⁻¹, and the [O III] line flux is strongly concentrated. Any substantial bulk motions must happen perpendicular to the line of sight. Overzier et al. (2013) argue that B1 is powered by an AGN that is undetected in X-rays.

Apart from the high velocity dispersion, B1 seems quite similar to J1155. Both show a high concentration of the line flux, surrounded by a very extended ($\gtrsim 20$ kpc) disk of much lower surface brightness with somewhat patchy structure. The [O III] luminosities are comparable, and J1155 is about twice as large (judging from our deep imaging data). Its Ly α luminosity estimated from *GALEX* far-UV data (Schirmer et al. 2016) is the same as that of B1. The diameter of the Ly α emission of J1155, and the accurate Ly α luminosity, are subject of our currently active *HST* proposal. J0113 has similar luminosity and extent as J1155, but its estimated Ly α luminosity is three times lower than that of B1.

We conclude that the recently discovered low-*z* LABs match high-*z* LABs in terms of luminosity and physical extent. Like B1, our targets host powerful AGN. At this point it is too early to speculate about the morphological similarities between B1 and J1155. While the formation of J0113 with its characteristic bipolar outflow and other signs of historic accretion events is quite clear cut (see Faucher-Giguère & Quataert 2012; Zubovas & King 2016), the formation and current state of J1155 remains

unclear and requires further observations (in particular optical line diagnostics and deeper data).

5.4. [O III] morphologies and AGN flickering

There is increasing evidence for AGN flickering (duty cycles lasting 10^{4-5} years, amplitudes of orders of magnitude), obtained by the identification of ionization echoes (e.g. Schawinski et al. 2010; Schirmer et al. 2016; Ichikawa et al. 2016; Keel et al. 2017), by means of statistical arguments and outflow rates (e.g. Schawinski et al. 2015; Sun et al. 2017), the transverse proximity effect in the Ly α forest (Kirkman & Tytler 2008, albeit on longer scales of 10^6 years), and also on the theoretical side (e.g. Hopkins & Quataert 2010; Novak et al. 2011; Sijacki et al. 2015; Zubovas & King 2016).

The typical time scales of AGN flickering are on the same order as the light crossing times of galaxy-scale outflows extending over 10 kpc and more. The optical appearance of these extended narrow-line regions is invariable over a human life time given their kinematic time-scale of Myrs, and the limited physical resolution of current instrumentation. However, because of their large extent, these nebulae reflect the recent history of the AGN, and this affects how we interpret their observed morphologies.

First of all, the effective recombination time scale for the O $^{++}$ ion is very short. Using the calculations of (Binette & Robinson 1987),

$$t_{\text{rec}}(\text{O}^{++}) = 158 \text{ yr} \left(\frac{n_e}{100 \text{ cm}^{-3}} \right)^{-1}. \quad (4)$$

Accordingly, the response of the [O III] line to a change in ionizing radiation can be considered instantaneous for observations with a physical resolution of ~ 1 kpc. An outward propagating wave of ionizing radiation (or a shut-down thereof) would alter the nebulae's surface brightness.

Secondly, we know from the *Changing Look* quasars (LaMassa et al. 2015; MacLeod et al. 2016; Runnoe et al. 2016) that AGN may change their line-of-sight obscurations on scales of years, affecting an ionization cone's opening angle (e.g. due to intervening dust, structural changes in the torus in response to a change of bolometric luminosity). Spin precession of the SMBH accretion disk happens on scales of 10^{3-7} years (Lu & Zhou 2005) and may cause illumination (ionization) patterns on a screen of gas extending over 10s of kpc.

Lastly, absence of line emission in some area does not imply absence of gas. These areas could be shielded from ionization by intervening dust. In turn, absence of line emission does not mean that there is no ionizing radiation; and AGN may well shine into empty volumes.

It is tempting to link the optical morphologies from our IFU data with the structural parameters of the central AGN derived from our X-ray analysis. Indeed, the consistencies are remarkable. From the X-ray data of J0113 we infer an AGN that is buried in a torus with a small opening angle. Accordingly, this AGN is able to photoionize gas within a relatively narrow ionization cone, only, matching the collimated bipolar outflow. However, the highest surface brightness of the line emission is lo-

cated in the central 2–4 kpc (upper right in Figure 4), showing that ionizing radiation can leak into other directions, too. In J1155, we find a weakly obscured AGN capable of ionizing gas over a wide solid angle, consistent with the optical nebula ionized at all azimuthal angles. However, our sample is highly limited (two), and as we cautioned above, the observable nebular morphologies are subject to outflow histories, and variabilities in obscuration, luminosity, and illumination direction.

5.5. Using scaling relations to test for long-term variability

Two possible explanations for the ionization deficits in LABs are deeply buried AGN, and time variable (faded) AGN (see Section 1). Our previous analysis of individual sources in Schirmer et al. (2016) was limited by poor knowledge of their X-ray obscurations. We could argue in favor of faded AGN for the sample as a whole, but not for individual sources. This limitation is overcome with hard X-ray (> 10 keV) data.

Currently, powerful ($L_X \sim 10^{44}$ erg s $^{-1}$) and Compton-thin AGN exist in both J0113 and J1155 (Section 3). To test for recent, long-term variability, we compare their X-ray luminosities against other proxies of AGN power that retain some memory of the AGNs' past. These proxies are mid-infrared (MIR) emission from circum-nuclear dust, and [O III] emission from the extended ionized gas. The built-in 'response' times of these 'echo screens' are caused by light-travel time from the nucleus, their intrinsic physical properties, and also their orientation along the line-of-sight (a response from the parts located closer to us would arrive sooner at our telescopes). In the following, we check whether these proxies bear any signs for substantial variability in both AGN over the last 10^{2-4} years.

5.5.1. The mid-infrared X-ray relation

Numerous studies have established a tight correlation between the MIR and X-ray luminosities in X-ray selected AGN; radiation from the central engine heats the dusty torus, which subsequently emits thermal radiation. This correlation is independent of AGN classifications (type-1/2, Compton thickness; see e.g. Gandhi et al. 2009; Ichikawa et al. 2012, 2017; Asmus et al. 2011, 2015). Rapid and prolonged fading of AGN, however, would move an individual AGN off the MIR X-ray correlation. Hönig & Kishimoto (2011) simulated the MIR response of a dusty torus to a finite pulse from the AGN, as a function of the torus' structural parameters. Ichikawa & Tazaki (2017) also estimated the typical cooling timescale of the dusty torus once the AGN is suddenly quenched and even considered the dust heating with the energy exchange by the gas. Accordingly, the thermal response of a torus may have decay times of 10–1000 years, depending on its thickness, and in addition to the time lag caused by the light travel time from the nucleus to the sublimation radius. We have presented observational data supporting such thermal echoes in Schirmer et al. (2016), pending confirmation by accurately measuring the X-ray obscurations.

Figure 7 shows scatter plots of the absorption corrected 2–10 keV luminosity versus MIR (12 μm and 22 μm) luminosity for the hard X-ray selected AGN of

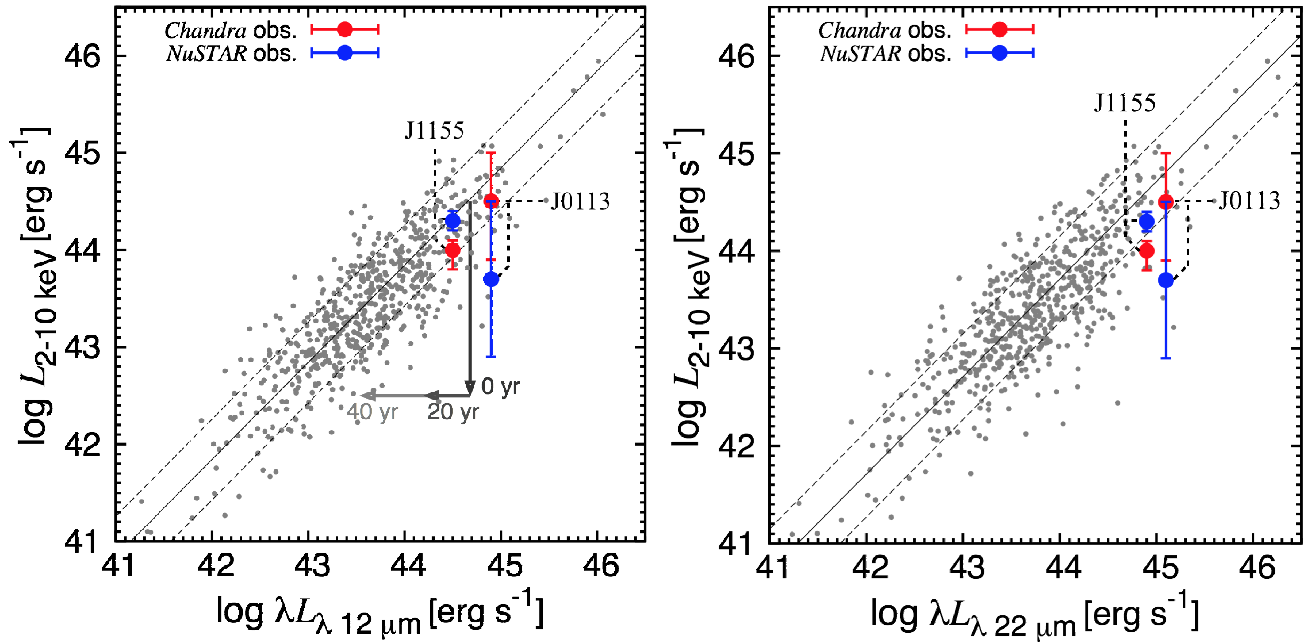


FIG. 7.— (Left) Correlation between the 2–10 keV and 12 μm luminosities. The solid line represents the regression line obtained from the Ichikawa et al. (2017) sample (gray points), and the dashed lines the 1σ envelope. The *NuSTAR* and *Chandra* data for our two LABs are shown by blue and red symbols, respectively, with 90% confidence error bars. The arrows illustrate the time evolution for a variable AGN. The vertical error indicates a sudden quenching by two orders of magnitude in X-ray luminosity. Subsequently, the 12 μm dust emission starts to respond, with indications of the 20 and 40 yr marks after the shutdown as estimated by Ichikawa & Tazaki (2017). More details about the time evolution is given in Section 5.5.1. (Right) The same as the left figure but for the 22 μm luminosity (without time evolution).

Ichikawa et al. (2017, gray dots). This is one of the most complete samples to date for the hard X-ray selected AGN. To make the plots, we converted the 14–195 keV luminosities to the 2–10 keV band, using a photon index of $\Gamma = 1.9$ (i.e., $L_{14-195 \text{ keV}}/L_{2-10 \text{ keV}} = 2.1$). The data for J0113 and J1155 are also shown, using their *WISE* W3 and W4 band fluxes (Wright et al. 2010) to estimate the 12 μm and 22 μm luminosities, respectively. The data for J1155 put it within the 1σ scattering of the reference sample. The *NuSTAR* observations of J0113 taken in 2016, however, deviate by one order of magnitude from the best-fit correlation, whereas its *Chandra* data taken in 2014 are in much better agreement with the reference sample. This illustrates the effect of rapid X-ray fading on this plot. Because dusty tori typically have pc-scales and delayed intrinsic response times (Hönig & Kishimoto 2011; Ichikawa & Tazaki 2017), the MIR flux of J0113 is not expected to change much just yet (and we used the single *WISE* measurement from 2010). Sparse long-term MIR monitoring of J0113 is worth-while, in particular if the X-ray flux continues to fade.

Since both AGN are still within the general scatter, we cannot infer long-term time (~ 10 –1000 yr) variability from the MIR X-ray relation. Note that we initially proposed seven targets to be observed with *NuSTAR*, covering a large range of *Chandra* fluxes. Only J0113 and J1155 were approved, because they are by far the X-ray brightest, maximizing chances for appreciable *NuSTAR* count rates. Therefore, highly significant deviations from the MIR X-ray scaling relation are not expected for these two targets, but could be present for the X-ray fainter LABs in our sample.

For clarity, we illustrate the simplified time evolution (arrows) after AGN quenching in the left panel of Figure 7. For this, we adopt an instantaneous decline by two orders of magnitude, supported by observational and theoretical data alike (Schawinski et al. 2010; Novak et al. 2011; Schirmer et al. 2016). The X-ray luminosity before the quenching is set to $\log L_{2-10 \text{ keV}} = 44.5$, the maximum luminosity we observe for J0113 and J1155. The 12 μm luminosity is estimated using the third equation in Table 3 of Ichikawa et al. (2017) for luminous AGN ($43 < L_{14-195 \text{ keV}} < 46$). Applying eq. (21) by Marconi et al. (2004) we derive the bolometric corrections for the 2–10 keV band, and then use Figure 3 of Ichikawa & Tazaki (2017) to estimate the cooling times. Note that Ichikawa & Tazaki (2017) assume a sudden and complete AGN shut down, whereas in reality it could take the AGN much longer to move back onto the general MIR X-ray correlation (depending on the radial dependence of the dust density Hönig & Kishimoto 2011).

5.5.2. Negligible effect from MIR emission lines

Particularly the W3 band, covering ~ 7.5 –17 μm^{10} , contains several emission lines (e.g., polycyclic aromatic hydrocarbon, [Si IV] 10.5 μm and [Ne II] 12.8 μm) from the more extended ($\gtrsim 100$ pc) star-forming and narrow-line regions than that of the torus ($\lesssim 10$ pc). These could contribute to the observed MIR flux, potentially diluting the expected MIR response from the dusty torus to a change in AGN luminosity. We can probe for this effect considering the X-ray MIR correlations obtained using

low and high spatial resolution observations: If the emission lines are bright, then the observed MIR flux would increase systematically with lower resolution, as more emission line flux is included from a larger volume around the AGN. However, this trend is not found when comparing the high-resolution study of Asmus et al. (2015) with the low-resolution study of Ichikawa et al. (2017) (see Figure 3 of Ichikawa et al. 2017). We conclude that the emission lines do not alter the MIR fluxes significantly.

Even if the W3 band was highly contaminated, one could still use the W4 band ($\sim 20\text{--}26\ \mu\text{m}$), which is less affected. The [O IV] line at $25.89\ \mu\text{m}$, which is a bright line in AGN spectra (Treyer et al. 2010), is lower than the X-ray / MIR luminosities by two orders of magnitude (e.g., Liu et al. 2014; Kawamuro et al. 2016). Unless the AGN and their kpc-scale surroundings in our low- z LABs are very different from typical AGN, MIR emission lines are not expected to skew the MIR X-ray scaling relations.

5.6. The [O III] X-ray relation

[O III] $\lambda 5007$ emission is another proxy commonly used to infer AGN power (e.g., Mulchaey et al. 1994). A typical [O III] nebular size observed in local Seyfert galaxies can reach several kpc (e.g., Schmitt et al. 2003; Bennert et al. 2006). In Figure 8, we compare our LABs with local AGN detected in the *Swift*/BAT 9-month catalog (Ueda et al. 2015). Both LABs have lower X-ray luminosities at a given [O III] luminosity than predicted from the average properties of the *Swift*/BAT sample, yet not at a level that would distinguish them as fading. The apparently high [O III] luminosity could simply be a fact of our selection (targetting optically over-luminous nebulae), and that our type of targets is not included in the commonly used SDSS AGN catalogs (the latter are incomplete concerning extreme sources, see Schirmer et al. 2013; Baron & Poznanski 2017). Nonetheless, for J0113 we know that it has been fading for the last two years. In addition, Ueda et al. (2015) report a lower [O III] to X-ray luminosity ratio on average for low scattering fraction AGN ($f_{\text{scat}} < 0.5\%$; green circles in Figure 8), to which J0113 belongs. J0113 is 10–50 times more luminous in [O III] than other low scattering AGN. This could simply be a consequence of poor statistics at the high luminosity end, or a consequence of variability (the [O III] X-ray relation decorrelates more easily than the MIR relation under AGN flickering due to the slower [O III] response). We conclude that, for our particular two targets, the [O III] X-ray relation does not bear conclusive evidence for AGN flickering.

6. SUMMARY

Using 20 ksec *NuSTAR* observations, we probed the hard X-ray emission of two recently discovered (Schirmer et al. 2016) low- z LABs, J0113 and J1155. We detect them in the observed 3–30 keV band on the 8σ and 21σ level, respectively. Adding *Chandra* archival data, we performed a broadband X-ray spectral analysis of the 0.5–30 keV band. The spectra were well reproduced with a base-line model consisting of an absorbed cut-off power-law, reflection components from distant, cold matter, and scattered emission. This is the most detailed X-ray analysis of AGN in any LABs published to

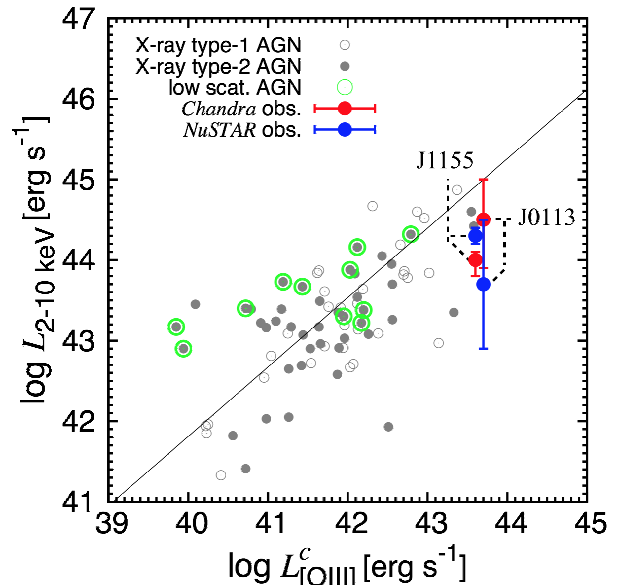


FIG. 8.— Correlation between the 2–10 keV and corrected [O III] luminosities. For clarity, J0113 is slightly shifted to the right. The solid line represents the regression line obtained by Ueda et al. (2015). The filled and un-filled circles denotes the X-ray type-1 ($\log(N_{\text{H}}/\text{cm}^{-2}) < 22$) and X-ray type-2 ($\log(N_{\text{H}}/\text{cm}^{-2}) \geq 22$) AGN, respectively. The superimposed green circles are attached to the low scattering AGN ($f_{\text{scat}} < 0.5\%$). Objects without detection of the $\text{H}\beta$ line were excluded from this plot because no extinction correction could be obtained for them.

date. It also shows that with *NuSTAR* one can strongly constrain the primary X-ray luminosity.

For J1155, we find a moderate scattering fraction of $f_{\text{scat}} = 1.2\%$. This shows that the AGN is not deeply buried in a torus, whose existence is suggested by the detection of the iron- $\text{K}\alpha$ line. The obscuration is moderate with $\log(N_{\text{H}}/\text{cm}^{-2}) \sim 22.8$. Hence, the AGN emission can indeed ionize the narrow line region that extends out to a radius of $\gtrsim 30$ kpc, over a wide opening angle. AGN ionization of the gas is required by its high $\log([\text{O III}]/\text{H}\beta)$ line ratio (Schirmer et al. 2013).

Regarding J0113, the torus may be highly developed. It reduces the scattering gas as inferred from the undetected scattered emission (upper limit $f_{\text{scat}} < 9.9\%$) as well as from the high column density ($\log(N_{\text{H}}/\text{cm}^{-2}) \sim 23.7$). This is consistent with the collimated bipolar outflow seen in the optical [O III] emission. However, the central 2–4 kpc also have high [O III] surface brightness, showing that ionizing radiation can leak out in other directions as well.

Our optical 3D spectroscopy with Gemini/GMOS (and imaging data from our previous work by Schirmer et al. 2016) reveals two very different systems. For J0113 we find multiple evidence for recurrent powerful outflow events over several 10 million years. The prominent bipolar outflow in J0113 is accelerating, as gas velocities increase with distance from the nucleus. This behaviour is best explained by AGN flickering (Zubovas & King 2016). J0113 is a prototypical example of the outflow formation process suggested by Faucher-Giguère & Quataert (2012), where hot buoyant gas breaks out along paths of least resistance, inflating kpc-scale superbubbles. The extended narrow-line re-

gion around J1155, on the other hand, reveals a very different morphology. It is more consistent with an advanced stage, where the remnants of multiple outflows are dispersing in the halo, passively illuminated/ionized by a current powerful accretion event. Deeper 3D spectra taken over a larger area, and covering more diagnostic emission lines, would allow us to better constrain the gas physics and formation histories of these two distinguished targets.

Common to both systems are low velocity dispersions of 100–150 km s⁻¹. In particular, the AGN themselves are not detectable in the line width maps. In case of J0113, severe dust extinction could be hiding more turbulent gas closer to the nucleus. Also, previous outflows could have cleared the escape paths for the current streams, reducing mechanical resistance and thus turbulence.

In terms of [O III] extent and luminosity, we find our low-*z* LABs indistinguishable from high-*z* LABs. J1155, in particular, resembles one of the best studied LABs (B1, see e.g., Francis et al. 2001; Palunas et al. 2004; Overzier et al. 2013) in many other respects, hosting a powerful AGN.

J0113 and J1155 fall within the intrinsic scatter of the MIR X-ray luminosity correlation, as well as within the [O III]-to-X-ray relation of the hard X-ray selected AGN (Ichikawa et al. 2017). J0113 has faded by a factor ~ 5 over two years of time between our *Chandra* and *NuSTAR* observations, but not enough to distinguish it with respect to the other AGN in these relations. It is worthwhile to monitor the MIR emission of J0113, roughly on a yearly basis, in particular if the X-ray luminosity continues fading. This would bear clues about the size and structure of its obscuring dusty torus, and the effect of long-term AGN variability on the intrinsic scatter of the MIR X-ray relation.

Our targets are among the most luminous [O III] emitters in the Universe, and at $z \sim 0.3$ they are easy targets for follow-up studies.

This work was financially supported by the Grant-in-Aid for JSPS fellows for young researchers (TK) and also for Scientific Research 40756293 (KI). Further financial support was provided by the Gemini Observa-

tory (TK). MS acknowledges support by the National Aeronautics and Space Administration through *Chandra* Award Number GO4-15110X issued by the *Chandra* X-ray Observatory Center, which is operated by the Smithsonian Astrophysical Observatory for and on behalf of the National Aeronautics Space Administration under contract NAS8-03060. This research has made use of the NASA/IPAC Infrared Science Archive, which is operated by the Jet Propulsion Laboratory, California Institute of Technology, under contract with the National Aeronautics and Space Administration.

Author contributions: TK reduced the *NuSTAR* and *Chandra* X-ray data, and performed the joint spectral analysis; TK and MS wrote the manuscript; MS performed the analysis of the 3D spectra, and led the *NuSTAR*, *Chandra* and Gemini proposals; JT reduced the Gemini 3D spectra and obtained the [O III] luminosities; RD obtained the velocity, velocity dispersion and line flux maps.

MS thanks Claudio Ricci, Daniel Asmus and Ai-Lei Sun for sharing their expertise on the subject.

This work is based on data from the *NuSTAR* mission, a project led by the California Institute of Technology, managed by the Jet Propulsion Laboratory, and funded by NASA. This research has made use of the *NuSTAR* Data Analysis Software (NuSTARDAS) jointly developed by the ASI Science Data Center and the California Institute of Technology.

This work made use of data supplied by the UK Swift Science Data Centre at the University of Leicester.

Based on observations made by the *Chandra* X-ray Observatory, and on data obtained from the *Chandra* Data Archive. We also made use of the software provided by the *Chandra* X-ray Center (CXC) in the application packages CIAO.

Based on observations obtained at the Gemini Observatory, which is operated by the Association of Universities for Research in Astronomy, Inc., under a cooperative agreement with the NSF on behalf of the Gemini partnership: the National Science Foundation (United States), the National Research Council (Canada), CONICYT (Chile), Ministerio de Ciencia, Tecnología e Innovación Productiva (Argentina), and Ministério da Ciência, Tecnologia e Inovação (Brazil).

REFERENCES

- Aihara, H., Allende Prieto, C., An, D., et al. 2011, *ApJS*, 193, 29
 Arnaud, K. A. 1996, in *Astronomical Society of the Pacific Conference Series*, Vol. 101, *Astronomical Data Analysis Software and Systems V*, ed. G. H. Jacoby & J. Barnes, 17
 Asmus, D., Gandhi, P., Smette, A., Hönig, S. F., & Duschl, W. J. 2011, *A&A*, 536, A36
 Asmus, D., Gandhi, P., Hönig, S. F., Smette, A., & Duschl, W. J. 2015, *MNRAS*, 454, 766
 Barger, A. J., Cowie, L. L., & Wold, I. G. B. 2012, *ApJ*, 749, 106
 Baron, D., & Poznanski, D. 2017, *MNRAS*, 465, 4530
 Basu-Zych, A., & Scharf, C. 2004, *ApJ*, 615, L85
 Bennert, N., Jungwiert, B., Komossa, S., Haas, M., & Chini, R. 2006, *A&A*, 459, 55
 Binette, L., & Robinson, A. 1987, *A&A*, 177, 11
 Bridge, C. R., Blain, A., Borys, C. J. K., et al. 2013, *ApJ*, 769, 91
 Brightman, M., & Nandra, K. 2011, *MNRAS*, 413, 1206
 Cardelli, J. A., Clayton, G. C., & Mathis, J. S. 1989, *ApJ*, 345, 245
 Ciardullo, R., Zeimann, G. R., Gronwall, C., et al. 2014, *ApJ*, 796, 64
 Dadina, M. 2008, *A&A*, 485, 417
 Davies, R. L., Schirmer, M., & Turner, J. E. H. 2015, *MNRAS*, 449, 1731
 Eguchi, S., Ueda, Y., Terashima, Y., Mushotzky, R., & Tueller, J. 2009, *ApJ*, 696, 1657
 Erb, D. K., Bogosavljević, M., & Steidel, C. C. 2011, *ApJ*, 740, L31
 Evans, P. A., Beardmore, A. P., Page, K. L., et al. 2009, *MNRAS*, 397, 1177
 Fardal, M. A., Katz, N., Gardner, J. P., et al. 2001, *ApJ*, 562, 605
 Faucher-Giguère, C.-A., & Quataert, E. 2012, *MNRAS*, 425, 605
 Forster, K., Harrison, F. A., Dodd, S. R., et al. 2014, *Proc. SPIE*, 9149, 91490R
 Francis, P. J., Williger, G. M., Collins, N. R., et al. 2001, *ApJ*, 554, 1001
 Gandhi, P., Horst, H., Smette, A., et al. 2009, *A&A*, 502, 457
 Gaskell, C. M., & Ferland, G. J. 1984, *PASP*, 96, 393
 Geach, J. E., Matsuda, Y., Smail, I., et al. 2005, *MNRAS*, 363, 1398
 Geach, J. E., Alexander, D. M., Lehmer, B. D., et al. 2009, *ApJ*, 700, 1
 Gehrels, N., Chincarini, G., Giommi, P., et al. 2005, *ApJ*, 621, 558

- Greene, J. E., Zakamska, N. L., Ho, L. C., & Barth, A. J. 2011, *ApJ*, 732, 9
- Haiman, Z., Spaans, M., & Quataert, E. 2000, *ApJ*, 537, L5
- Harrison, F. A., Craig, W. W., Christensen, F. E., et al. 2013, *ApJ*, 770, 103
- Harrison, C. M., Alexander, D. M., Mullaney, J. R., & Swinbank, A. M. 2014, *MNRAS*, 441, 3306
- Henry, A., Scarlata, C., Martin, C. L., & Erb, D. 2015, *ApJ*, 809, 19
- Holt, J., Tadhunter, C. N., Morganti, R., & Emonts, B. H. C. 2011, *MNRAS*, 410, 1527
- Hönig, S. F., & Kishimoto, M. 2011, *A&A*, 534, A121
- Hopkins, P. F. & Quataert, E. 2010, *MNRAS*, 407, 1529
- Ichikawa, K., Ueda, Y., Terashima, Y., et al. 2012, *ApJ*, 754, 45
- Ichikawa, K., Ueda, J., Shidatsu, M., Kawamuro, T., & Matsuoka, K. 2016, *PASJ*, 68, 9
- Ichikawa, K., Ricci, C., Ueda, Y., et al. 2017, *ApJ*, 835, 74
- Ichikawa, K., & Tazaki, R. 2017, *ApJ*, 844, 21
- Kalberla, P. M. W., Burton, W. B., Hartmann, D., et al. 2005, *A&A*, 440, 775
- Kawamuro, T., Ueda, Y., Tazaki, F., Ricci, C., & Terashima, Y. 2016, *ApJS*, 225, 14
- Keel, W. C., White, III, R. E., Chapman, S., & Windhorst, R. A. 2009, *AJ*, 138, 986
- Keel, W. C., Lintott, C. J., Maksym, W. P., Bennert, V. N., Chojnowski, S. D., Moiseev, A., Smirnova, A., Schawinski, K., Sartori, L. F., Urry, C. M., Pancoast, A., Schirmer, M., Scott, B., Showley, C., & Flatland, K. 2017, *ApJ*, 835, 256
- King, A. R., Zubovas, K., & Power, C. 2011, *MNRAS*, 415, L6
- Kirkman, D., & Tytler, D. 2008, *MNRAS*, 391, 1457
- Kollmeier, J. A., Zheng, Z., Davé, R., et al. 2010, *ApJ*, 708, 1048
- LaMassa, S. M., Cales, S., Moran, E. C., et al. 2015, *ApJ*, 800, 144
- Laursen, P. & Sommer-Larsen, J. 2007, *ApJ*, 657, L69
- Liu, G., Zakamska, N. L., Greene, J. E., Nesvadba, N. P. H., & Liu, X. 2013, *MNRAS*, 436, 2576
- Liu, T., Wang, J.-X., Yang, H., Zhu, F.-F., & Zhou, Y.-Y. 2014, *ApJ*, 783, 106
- Lu, J.-F., & Zhou, B.-Y. 2005, *ApJ*, 635, L17
- MacLeod, C. L., Ross, N. P., Lawrence, A., et al. 2016, *MNRAS*, 457, 389
- Magdziarz, P., & Zdziarski, A. A. 1995, *MNRAS*, 273, 837
- Marconi, A., Risaliti, G., Gilli, R., et al. 2004, *MNRAS*, 351, 169
- Matsuda, Y., Yamada, T., Hayashino, T., et al. 2004, *AJ*, 128, 569
- Matsuda, Y., Yamada, T., Hayashino, T., Yamauchi, R., & Nakamura, Y. 2006, *ApJ*, 640, L123
- Matsuda, Y., Yamada, T., Hayashino, T., et al. 2011, *MNRAS*, 410, L13
- Matt, G., Perola, G. C., & Piro, L. 1991, *A&A*, 247, 25
- Meinköhn, E. & Richling, S. 2002, *A&A*, 392, 827
- Mulchaey, J. S., Koratkar, A., Ward, M. J., et al. 1994, *ApJ*, 436, 586
- Mullaney, J. R., Alexander, D. M., Fine, S., et al. 2013, *MNRAS*, 433, 622
- Nesvadba, N. P. H., Lehnert, M. D., Eisenhauer, F., et al. 2006, *ApJ*, 650, 693
- Nilsson, K. K., Fynbo, J. P. U., Møller, P., Sommer-Larsen, J., & Ledoux, C. 2006, *A&A*, 452, L23
- Novak, G. S., Ostriker, J. P., & Ciotti, L. 2011, *ApJ*, 737, 26
- Osterbrock, D. E., & Ferland, G. J. 2006, *Astrophysics of gaseous nebulae and active galactic nuclei*, 2nd. ed. by D.E. Osterbrock and G.J. Ferland. Sausalito, CA: University Science Books, 2006
- Overzier, R. A., Nesvadba, N. P. H., Dijkstra, M., et al. 2013, *ApJ*, 771, 89
- Palunas, P., Teplitz, H. I., Francis, P. J., Williger, G. M., & Woodgate, B. E. 2004, *ApJ*, 602, 545
- Prescott, M. K. M., Kashikawa, N., Dey, A., & Matsuda, Y. 2008, *ApJ*, 678, L77
- Prescott, M. K. M., Momcheva, I., Brammer, G. B., Fynbo, J. P. U., & Møller, P. 2015, *ApJ*, 802, 32
- Rivera-Thorsen, T. E., Hayes, M., Östlin, G., et al. 2015, *ApJ*, 805, 14
- Rosdahl, J. & Blaizot, J. 2012, *MNRAS*, 423, 344
- Roy, I., Shu, C.-W., & Fang, L.-Z. 2010, *ApJ*, 716, 604
- Runnoe, J. C., Cales, S., Ruan, J. J., et al. 2016, *MNRAS*, 455, 1691
- Schawinski, K., Evans, D. A., Virani, S., et al. 2010, *ApJ*, 724, L30
- Schawinski, K., Koss, M., Berney, S., & Sartori, L. F. 2015, *MNRAS*, 451, 2517
- Schirmer, M., Diaz, R., Holmjem, K., Levenson, N. A., & Winge, C. 2013, *ApJ*, 763, 60
- Schirmer, M., Malhotra, S., Levenson, N. A., et al. 2016, *MNRAS*, 463, 1554
- Schmitt, H. R., Donley, J. L., Antonucci, R. R. J., Hutchings, J. B., & Kinney, A. L. 2003, *ApJS*, 148, 327
- Sijacki, D., Vogelsberger, M., Genel, S., et al. 2015, *MNRAS*, 452, 575
- Steidel, C. C., Adelberger, K. L., Shapley, A. E., et al. 2000, *ApJ*, 532, 170
- Storey, P. J., & Zeppen, C. J. 2000, *MNRAS*, 312, 813
- Storey, P. J., & Sochi, T. 2015, *MNRAS*, 446, 1864
- Sun, A.-L., Greene, J. E., & Zakamska, N. L. 2017, *ApJ*, 835, 222
- Taniguchi, Y., & Shioya, Y. 2000, *ApJ*, 532, L13
- Trebtsch, M., Verhamme, A., Blaizot, J., & Rosdahl, J. 2016, *A&A*, 593, A122
- Treyer, M., Schiminovich, D., Johnson, B. D., et al. 2010, *ApJ*, 719, 1191
- Ueda, Y., Eguchi, S., Terashima, Y., et al. 2007, *ApJ*, 664, L79
- Ueda, Y., Hashimoto, Y., Ichikawa, K., et al. 2015, *ApJ*, 815, 1
- Urry, C. M., & Padovani, P. 1995, *PASP*, 107, 803
- Verhamme, A., Schaerer, D., & Maselli, A. 2006, *A&A*, 460, 397
- White, R. L., Becker, R. H., Helfand, D. J., & Gregg, M. D. 1997, *ApJ*, 475, 479
- Wold, I. G. B., Barger, A. J., & Cowie, L. L. 2014, *ApJ*, 783, 119
- Wright, E. L., Eisenhardt, P. R. M., Mainzer, A. K., et al. 2010, *AJ*, 140, 1868
- Xu, W., Wu, X.-P., & Fang, L.-Z. 2011, *MNRAS*, 418, 853
- Yang, H., Malhotra, S., Gronke, M., et al. 2016, *ApJ*, 820, 130
- Zubovas, K., & King, A. 2016, *MNRAS*, 462, 4055